La sottoscritta Giulia Cappelli, in qualità di co-autrice del lavoro seguente:

Titolo: Computational and experimental validation of phthalocyanine and hypericin as effective SARS-CoV-2 fusion inhibitors
Autori: Alice Romeo, Giulia Cappelli, Federico Iacovelli, Vittorio Colizzi and Mattia Falconi
Rivista: *Journal of Biomolecular Structure and Dynamics*
Volume: 42
Fascicolo: 8
Pagine: 3920–3934
DOI: 10.1080/07391102.2023.2216276
Codice ISI: WOS:000995335900001
Codice Scopus: 2-s2.0-85160793020
Link alla VoR sul sito dell'Editore:
https://www.tandfonline.com/doi/full/10.1080/07391102.2023.2216276

autocertifica

che la copia allegata a questa dichiarazione coincide con la versione accettata per la pubblicazione (Author's Accepted Manuscript, AAM).

Dr^ssa^ Giulia Cappelli

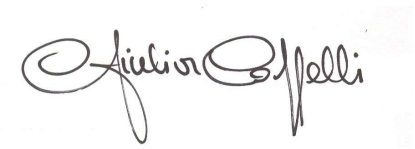

Computational and experimental validation of phthalocyanine and hypericin as effective SARS-CoV-2 fusion inhibitors

Alice Romeo[1#], Giulia Cappelli[2#], Federico Iacovelli[1], Vittorio Colizzi[3] and Mattia Falconi[1]*

[1] Department of Biology, University of Tor Vergata, Rome, Italy.

[2] Istituto per i Sistemi Biologici, Consiglio Nazionale delle Ricerche, Montelibretti, Rome, Italy.

[3] University of Tor Vergata, Rome, Italy.

[*]Correspondence: falconi@uniroma2.it

[#]These authors contributed equally to this work and should be considered co-first authors.

KEYWORDS: SARS-CoV-2, hypericin, phthalocyanine, fusion inhibitors, molecular simulations, pseudovirus antiviral assay

ABSTRACT. Phthalocyanine and hypericin have been previously identified as possible SARS-CoV-2 Spike glycoprotein fusion inhibitors through a virtual screening procedure. In this paper, atomistic simulations of metal-free phthalocyanines and atomistic and coarse-grained simulations of hypericins, placed around a complete model of the Spike embedded in a viral membrane, allowed to further explore their multi-target inhibitory potential, uncovering their binding to key protein functional regions and their propensity to insert in the membrane. Following computational results, pre-treatment of a pseudovirus expressing the SARS-CoV-2 Spike protein with low compounds concentrations resulted in a strong inhibition of its entry into cells, suggesting the activity of these molecules should involve the direct targeting of the viral envelope surface. The combination of computational and *in vitro* results hence supports the role of hypericin and phthalocyanine as promising SARS-CoV-2 entry inhibitors, further endorsed by literature reporting the efficacy of these compounds in inhibiting SARS-CoV-2 activity and in treating hospitalized COVID-19 patients.

INTRODUCTION

Almost three years after its first isolation from a cluster of patients with pneumonia in Wuhan (China) on December 2019, the Severe Acute Respiratory Syndrome Coronavirus 2 (SARS-CoV-2), responsible for the COVID-19 pandemic, still represents a threat to the world population with over 662 million confirmed cases and over 6.7 million deaths reported globally (as of 15 January 2023, https://www.who.int/emergencies/diseases/novel-coronavirus-2019/situation-reports). Despite the undeniable relevance and efficacy of vaccination as a therapeutic measure against this pathogen, continuous research of additional antivirals is still required, considering the rapid transmission of this virus, the development of new concerning variants with the consequent high risk of reinfection in vaccinated subjects, the absence of protection for immunocompromised patients and the lack of worldwide availability of vaccines, particularly in developing countries (Telenti et al., 2021).

During the pandemic, the Spike (S) glycoprotein has emerged as the main virulence factor of SARS-CoV-2 since it is responsible for cell tropism and infectivity of the virus and can induce host immunopathogenesis, acting as a critical regulator of virus infection and disease outcomes (Saadi et al., 2021). Consequently, this protein also represents the main target of therapeutics aimed at preventing virus entry into host cells and acting in the first stages of the COVID-19 disease. In particular, worldwide research has focused on discovering compounds interacting with the S protein and preventing its attachment to the cellular ACE2 receptor or its subsequent conformational transitions, which are crucial to initiate viral fusion to the host cell (Xiu et al., 2020).

Based on previous research carried out for the human Respiratory Syncytial Virus (RSV) Fusion (F) glycoprotein (Battles et al., 2016; Battles & McLellan, 2019; Lopes et al., 2020), we suggested that targeting an internal cavity of the SARS-CoV-2 S glycoprotein in prefusion conformation could be a valuable approach for hindering its prefusion to postfusion transition, consequently blocking virus entry into the host cells (Romeo et al., 2020). A virtual screening, performed on a set of about 8000 FDA drugs, identified the metal-free 31h-phthalocyanine and hypericin as the compounds showing the highest affinity for this internal pocket, suggesting a possible role of these molecules as SARS-CoV-2 fusion inhibitors (Romeo et al., 2020). Hypericin is mainly derived from plants of the genus *Hypericum*, particularly the *Hypericum perforatum* (St. John's Wort), which is widely known for its antidepressant properties (Karioti & Bilia, 2010; Kubin et al., 2005), while phthalocyanine compounds are commonly used as photoconductive materials and catalysts (Sorokin, 2013; Wright, 2001). Considering their photodynamic properties, both compounds have also been evaluated as oxidizing agents in the photodynamic therapy of cancer, since in combination with light they can efficiently induce apoptosis and/or necrosis of tumor cells, and also as a treatment for microbial infections (Karioti & Bilia, 2010; Kubin et al., 2005; Santos et al., 2020; Wu et al., 2023). Given their

tendency to aggregate in physiological environments, different drug delivery systems have been investigated for hypericin or phthalocyanine derivatives, to improve their bioactivity and favour their possible translation to clinical evaluation settings (Santos et al., 2020; Wu et al., 2023).

Interestingly, the antiviral activity of both compounds or their derivatives against enveloped viruses has been reported in several studies (Degar et al., 1992; Korneev et al., 2019; Kubin et al., 2005; Nikolaeva-Glomb et al., 2017; Smetana et al., 1994; Stevenson & Lenard, 1993; Wu et al., 2023). For example, hypericin and different phthalocyanine derivatives were shown to prevent HIV infections by interfering with gp120 binding and fusion to the host cell (François et al., 2009; Lenard et al., 1993; Vzorov et al., 2003). Hypericin was also reported to interfere with HIV replication by targeting the viral capsid, inducing photochemical alterations of capsid proteins and increasing the rigidity of this region (Degar et al., 1992). This compound can also inhibit the avian coronavirus IBV through a mechanism that mostly involves the inhibition of virus-induced cellular apoptosis (Chen, Feng, et al., 2019; Chen, Muhammad, et al., 2019). Nevertheless, the antiviral activity of hypericin and phthalocyanine was mostly considered to be light-dependent (Hudson et al., 1993; Korneev et al., 2019; Kubin et al., 2005; Smetana et al., 1994), limiting their *in vivo* therapeutic applicability.

After the publication of our results (Romeo et al., 2020), a putative role of both phthalocyanine and hypericin as SARS-CoV-2 inhibitors has been reported in literature. A clinical trial showed that the use of a phthalocyanine-containing mouthwash helped in reducing symptoms and hospitalization time for COVID-19 patients, with no side effects reported (da Silva Santos et al., 2021). Interestingly, in this study the virucidal activity was observed in the dark and with an iron phthalocyanine known to have poor photochemical properties, suggesting that a different mechanism rather than photoexcitation should be involved. Concerning hypericin, recent studies demonstrated that this compound can inhibit SARS-CoV-2 activity without affecting cell viability (Delcanale et al., 2022; Jang et al., 2021; Matos et al., 2022; Mohamed et al., 2022), showing an IC_{50} of 559 pg/mL (Mohamed et al., 2022) and 19.34 μM (Jang et al., 2021), the latter close to the clinical drug remdesivir (10.09 μM). Hypericin is also active against the SARS-CoV-2 Alpha (B.1.1.7 lineage), Beta (B.1.351 lineage) and Delta (B.1.617.2 lineage) variants of concern (Mohamed et al., 2022). Furthermore, *H. perforatum* extracts containing hypericin as the main component were shown to induce a strong inhibitory effect on SARS-CoV-2 (Bajrai et al., 2022; Mohamed et al., 2022). The observed effects were stronger when the virus was pre-treated with the extracts before cell infection, indicating that the antiviral mechanism should take place on the viral surface. Indeed, direct binding of hypericin to SARS-CoV-2 viral particles was observed in a recent study using fluorescent microscopy, most likely occurring at the level of the lipid envelope (Delcanale et al., 2022).

Considering this evidence, we hypothesized that, when diffusing over the SARS-CoV-2 envelope, these compounds could exert a concerted and non-specific antiviral activity, potentially acting on multiple viral targets to interfere with virus attachment and fusion. Indeed, computational studies suggested the presence of a high-affinity interaction between hypericin and the S RBD (Smith & Smith, 2020) and reported the propensity of this compound to insert within lipid bilayers (Gattuso et al., 2017).

Therefore, we explored the multi-target potential of a metal-free phthalocyanine and of hypericin through Gaussian accelerated Molecular Dynamics (GaMD), an advanced sampling method allowing unconstrained enhanced sampling of biomolecular systems, which has been successfully applied to uncover ligand binding pathways during simulations (Miao et al., 2015; J. Wang et al., 2021). Simulated systems include a complete model of S embedded in a viral membrane (Woo et al., 2020), in the presence and absence of several molecules of each proposed inhibitor, randomly placed in the solvent.

To balance the limitations of atomistic simulations of these large macromolecular systems, which allow the sampling of molecules' motions for only on a limited timescale, an equivalent SARS-CoV-2 envelope portion model was also modelled and simulated at Coarse-Grained (CG) resolution. Only hypericin was selected as an inhibitory molecule at this stage, being the best protein-membrane interactor identified in the atomistic trajectories. Despite the approximations introduced, recent results showed that the prediction of protein-ligand interactions in CG simulations, without *a priori* knowledge of the binding site, has reached an accuracy approaching that of atomistic simulations (Souza et al., 2020). Moreover, recently CG models of the entire SARS-CoV-2 virion were separately developed by the groups of Amaro, Marrink and Tieleman (Pezeshkian et al., 2021; B. Wang et al., 2022; Yu et al., 2021). To support the obtained computational results and validate the efficacy of phthalocyanine and hypericin in blocking virus fusion, experimental tests have also been carried out using an *in vitro* model of infection of a HEK293T/ACE2 cellular line with a Pseudotyped Luciferase Lentivirus, expressing the SARS-CoV-2 S glycoprotein on its envelope surface.

MATERIALS AND METHODS

Computational methods

Gaussian accelerated MD simulations

Gaussian accelerated MD (GaMD) simulations (Miao et al., 2015) were performed using a complete model of the wild-type SARS-CoV-2 S glycoprotein in prefusion conformation, with the RBDs in closed configuration and including glycosylation and palmitoylation sites (Woo et al., 2020). Protein insertion in a 230x230 Å membrane and generation of final topology and coordinate files were carried

out using the Membrane Builder tool of the CHARMM-GUI interface (https://www.charmm-gui.org/) (Jo et al., 2008). The CHARMM36m force field for proteins (Huang et al., 2016), lipids (Klauda et al., 2010), and carbohydrates (Guvench et al., 2011) was used to parametrize the protein-membrane system. Membrane composition mimics that of a viral envelope, including cholesterol (30%), 3-palmitoyl-2-oleoyl- D-glycero-1-phosphatidylcholine (6%), 2,3 dipalmitoyl-D-glycero-1-phosphatidylcholine (4%), 3-palmitoyl-2-oleoyl-D-glycero-1-phosphatidylethanolamine (18%), 2,3 dipalmitoyl-Dglycero-1-phosphatidylethanolamine (12%), 3-palmitoyl-2-oleoyl-D-glycero-1-phosphatidylserine (6%), 2,3 dipalmitoyl-D-glycero-1-phosphatidylserine (4%), and sphingomyelin d18;1/16;0 (20%) (Woo et al., 2020). Three S-membrane models have been simulated: I) a reference without the two compounds (S-REF), II) a system in the presence of several phthalocyanine molecules (S-PHT), III) a system in the presence of several hypericin molecules (S-HYP). The molecules were randomly inserted around the S protein and the membrane using the Packmol program (Martínez et al., 2009). The compounds' structures were retrieved from the PubChem database (Kim et al., 2021), and their parameters were generated using the CGenFF program (https://cgenff.umaryland.edu) and the CHARMM general force field (Vanommeslaeghe et al., 2010). Each system was inserted in a rectangular box filled with TIP3P water molecules (Jorgensen et al., 1983) and neutralized with 0.15 M of NaCl ions. The final reference system included 2.087.887 atoms.

To remove unfavourable interactions, structures were minimized in ten runs, each including 2000 steps. A constraint of 20.0 kcal/mol was initially applied on each atom, sequentially halved in the subsequent runs, and finally removed in the last one. Minimized systems were then thermalized in a canonical ensemble (NVT) using a timestep of 1.0 fs, gradually increasing the temperature from 0 to 310 K every 30.0 ps using Langevin dynamics (Goga et al., 2012) and applying a constraint of 5.0 kcal/mol on protein and membrane atoms. Then, systems were equilibrated in an anisotropic NPT (NPT-A) ensemble using the Nosè–Hoover Langevin piston method (Feller et al., 1995; Martyna et al., 1994) and a constant pressure of 1.0 atm, gradually releasing the constraints applied on the protein and membrane every 250 ps during a 2250 ps run. Finally, the timestep was increased to 2.0 fs and the systems were simulated for 10.0 ns using classical MD before starting 150 ns of dual-boost GaMD (Miao et al., 2015). GaMD simulation included 2.0 ns of classical MD preparation, 50.0 ns of GaMD equilibration, and 100 ns of GaMD production. The upper and lower limits for the standard deviation of the total boost potential were maintained at the default value of 6.0 kcal/mol. Electrostatic interactions were calculated using the PME method (Darden et al., 1993), while the cut-off for non-bonded interactions was set to 12.0 Å. All simulations have been performed using the NAMD 2.13 software (Phillips et al., 2005) on the ENEA CRESCO6 HPC cluster (Iannone et al., 2019).

Coarse-grained MD simulations

Atomistic structure of hypericin has been modelled and parametrized at CG resolution following the Martini 3 force field building-block approach. The parametrization workflow is described in more detail in the Supplemental material. The tools *martinize2* (https://github.com/marrink-lab/vermouth-martinize) and *Insane* (Wassenaar et al., 2015) (https://github.com/Tsjerk/Insane) were used to build a CG model of a portion of the SARS-CoV-2 envelope, including the S glycoprotein inserted in membrane and surrounded by hypericin molecules. The atomistic SARS-CoV-2 S model used as input was the same structure used in GaMD simulations, and its CG model was generated following Martini 3 guidelines (Grünewald et al., 2021). An elastic network was automatically generated by the *martini2* tool based on the input structure protein. The CG protein was inserted in membrane using the *insane* tool, and then the system was solvated using Martini 3 water beads and 0.15 M of NaCl ions. Membrane composition was chosen to mimic the viral envelope (POPC: 55.0%, POPE: 25.0%, POPI: 10.0%, POPS: 2.0%, CHOL: 6.0%, CDL2= 2.0%) (Pezeshkian et al., 2021). Coarse-grained hypericin molecules were randomly distributed in the solvent around the protein using the *insert-molecules* tool of GROMACS (Abraham et al., 2015). A reference system without hypericin molecules was also generated. All simulations have been performed using the Martini 3 force field (Souza et al., 2021) and the GROMACS 2020 software (Abraham et al., 2015) on the ENEA CRESCO6 HPC cluster (Iannone et al., 2019).

Starting structures were initially minimized for 5000 steps using the steepest descent integrator and applying positional restraints of 1000 kj/mol · nm^2 on protein, ligands, and membrane polar heads beads. Then, further 5000 steps of steepest descent minimization were carried out without positional restraints. Equilibration in an NPT ensemble was carried out in 30.0 ns using a timestep of 20.0 fs. During the first 20.0 ns, restraints applied on protein, ligands and membrane polar heads beads were gradually halved from 1000 to 100 kj/mol · nm^2 every 5.0 ns. Then, a final 10.0 ns equilibration was performed by applying a 100 kj/mol · nm^2 restraint only on protein and ligands beads. The Parrinello-Rahman barostat (Parrinello & Rahman, 1981) was used to maintain the pressure to 1.0 atm, and the velocity-rescaling thermostat (Bussi et al., 2007) to fix the temperature to 310.0 K. Separate coupling groups were defined for the solute (protein, membrane, hypericin molecules) and the solvent. The LINCS algorithm (Hess et al., 1997) was employed to constrain covalent bonds involving hydrogen atoms, setting the *lincs-order* parameter to 8.

To randomize the initial positions of the hypericin molecules and generate different starting structures for the protein-membrane-hypericin system, the last frame obtained from this first equilibration phase was used as input for a 100 ns simulation, where GROMACS discoidal flat-bottomed position

restraints were applied (https://manual.gromacs.org/documentation/2019/reference-manual/functions/restraints.html). This type of restraint can be used to confine defined particles to only a part of the simulation volume, by using a harmonic force. This way, hypericin molecules were allowed to freely move in the solvent and randomize their positions without interacting with the protein or membrane before the beginning of the production phase. The discoidal flat-bottomed potential was defined through a cylinder potential of radius 2.0 nm and a layer potential of 5.0 nm in thickness, both parallel to the z-axis and centered around each hypericin. A harmonic force constant of 100 kj/mol · nm^2 was applied to keep the hypericin molecules within the discoidal volume defined. A small restraint of 50 kj/mol · nm^2 was also applied on S protein beads to prevent the structure from exiting the disk of potential generated. From the obtained trajectory, 14 different frames were randomly extracted and used as starting structures for replicated simulations of the system. For each replica, 5000 steps of steepest descent minimization and 10.0 ns of equilibration without restraints were carried out before starting a 10.0 μs production simulation. 5 replicas of the reference system without hypericin molecules were also simulated for 10.0 μs each, starting from the final structure obtained from the previous equilibration steps.

Trajectory analyses

Membrane thickness was evaluated using the VMD MEMBPLUGIN Tool (Guixà-González et al., 2014) and 2D thickness maps were generated using an in-house Python script. Radial distribution functions (RDFs) for phthalocyanine and hypericin were calculated using the GROMACS 2020 software (Abraham et al., 2015), setting S Cα atoms as the reference set of positions. The binding persistence of molecules with each S domain was calculated in VMD (Humphrey et al., 1996) through a custom Tcl script, using a distance threshold of 4.0 Å to identify a contact. Principal Component Analysis (PCA) (Amadei et al., 1993) calculations were performed on S Cα atoms using GROMACS 2020 (Abraham et al., 2015). Cross-correlation plots were generated using custom Python scripts. Salt bridges were calculated through the VMD Salt Bridges Tool. Occupancy of the hypericin molecules on the S surface during the CG trajectories was calculated using the VMD Volmap tool as described in http://cgmartini.nl/index.php/2021-martini-online-workshop/tutorials/563-7-protein-small-molecule-binding. S bending angles were calculated using an in-house Tcl script in VMD and plotted through a custom Python script. Images were generated using the VMD software (Humphrey et al., 1996). For CG model visualization, protein and membrane CG bonds were calculated in VMD using the *cg_bonds* tool (http://cgmartini.nl/index.php/tools2/visualization).

Experimental methods

Cell lines and compounds

HEK293T/ACE2 (CSC-RO0641/Creative Biogene) cell lines have been chosen since they express the ACE2 human receptor, used by the SARS-CoV-2 S glycoprotein to contact the host cells. The stock purchased corresponds to a single aliquot of $5x10^6$ cells/ml. Cells were first stored in liquid nitrogen and then removed and thawed in a 37 °C water bath. The thawing procedure was rapid and careful to avoid any kind of contamination. In a biosafety cabinet, cells were transferred into a 15 ml conical tube containing 9 ml of pre-warmed culture medium (without puromycin) and then centrifuged at ~125 x g for 5~7' at room temperature. After that, the supernatant was removed and cells were resuspended in 1 ml culture medium (without puromycin). Subsequently, cells were transferred to a T25 flask containing 5 ml pre-warmed culture medium (without puromycin) and incubated at 37°C with 5% of CO_2. Once a 90% of confluence was reached, the medium culture was removed and the monolayer was washed with 5-10 ml of phosphate-buffered saline (PBS). To obtain a sufficient amount of cells, 2 ml of 0.25% Trypsin-EDTA solution was added to the flask and incubated at 37°C for 5~15' until the cells dissociated. After that trypsin was neutralized with 8 ml of complete growth medium and cells were transferred to a fresh T75 flask, adding fresh complete growth medium to a total volume of 10 ml. Then, cells were incubated at 37°C with 5% of CO_2.
The 31h-phthalocyanine (Product code: 253103) and hypericin (Product code: 00190585) compounds have been purchased from Sigma-Aldrich (https://www.sigmaaldrich.com).

Pseudovirus

The SARS-CoV-2 S Pseudotyped Luciferase Lentivirus (CoV2-002 /Creative Biogene) is an HIV-based luciferase lentivirus pseudotyped with the SARS-CoV-2 full-length S protein. The virus was produced with three plasmids: one containing the gag/pol genes, one containing the Firefly luciferase reporter gene, and one containing the SARS-CoV-2 full-length S protein encoding sequence. The stock purchased corresponds to aliquots of $1x10^7$ TU/ml and must be stored at -80°C. This engineered pseudovirus cannot replicate and infect the cells since it lacks the viral genetic material that codes for virulence factors, allowing a safer manipulation if compared with the SARS-CoV-2 virus. In addition, the expression of viral glycoproteins on its outer membrane allows to evaluate the initial process of infection and interaction between the host and the pathogen.

Luciferase assay and infection procedure

The presence of the luciferase reporter gene allows to measure the amount of viral particles infecting the cells, since it can be transcribed only after virus entry. The luciferase was detected by the highly sensitive ONE-Glo™ test (Promega E6120) and measured through a luminometer. Initially, a series

of preliminary experiments have been performed to establish the best culture and infection conditions using different multiplicity of infections (MOI 5:1/ 10:1 / 20:1 / 50:1), to establish which virus:cell ratio guaranteed the maximum efficacy of infection and the minimum cell mortality. Furthermore, different times of infection (7h / 12h / 24h) and different times of Luciferase detection (16h / 24h) were chosen. According to these preliminary experiments, 10:1 was identified as the best MOI for the infection, and 24h after the infection as the proper time for the Luciferase detection.

Cellular cytotoxicity

HEK293T/ACE2 (CSC-RO0641 /Creative Biogene) were plated at 10^4 cells in 96 wells plated and incubated overnight to obtain confluent monolayers. The following day, distinct concentrations of the candidate compounds (ranging from 12.50 μg/μl to 0.005 μg/μl) were added to the cells culture in triplicate, and different times of incubation were analyzed (from 30 min to 4 h). After incubation, 25 μl of fresh 5 mg/ml PBS-diluted MTT [3-(4,5-Dimethylthiazol-2yl)-2,5-diphenyl-tetrazolium-bromid] were applied directly to each well and incubated at 37 °C/ 5% CO_2/1 h. Subsequently, MTT suspensions were removed, cells were lysed by adding 50 μL/well DMSO, and further incubated for 3–5 min at room temperature. Finally, measurements were performed at 562 nm in a photometer, and the percentage (%) of cell survival was calculated compared to the solvent control DMSO.

Reactive Oxygen Species detection

ROS generation was analysed, as previously described (Greco et al., 2012) by loading cells with 10 μM of the cell-permeant fluorescent indicator 2', 7'-dichlorofluorescein diacetate (H_2DCFDA) (Molecular Probes) for 60 minutes at 37 °C in the dark. Upon cleavage of the acetate groups by intracellular esterases and oxidation, the non-fluorescent H_2DCFDA is converted to the highly fluorescent 2', 7'-dichlorofluorescein (DCF). DCF fluorescence intensity is proportional to the intracellular amount of ROS produced (Sen & Packer, 1996). After labelling, 10^6 HEK293ACE2 cells were washed twice with PBS, centrifuged for 10 minutes at 580 g, resuspended in PBS buffer, and stimulated with two different concentrations of hypericin or phthalocyanine (C1:0.78 μg/ml and C2:0.005 μg/ml). ROS production was determined at 45 minutes after compounds stimulation by fluorimetric measurement of fluorescence (excitation 488 nm; emission 530 nm). Fluorescence emission was monitored using a Perkin Helmer LS50B Luminescence Spectrometer. Negative (untreated cells) and positive (cells treated with 100 μM menadione for one hour) controls have been included in both experimental conditions. To study the possible interference of light on hypericin and phthalocyanine antiviral activity, both for the cytotoxic assay and for the ROS detection, a series of five parallel experiments have been performed under BSLII cabinet in usual conditions (with light

on, at an intensity of 1187.1 Lux for 1 minute) and in dark conditions (light off). These two conditions were chosen to evaluate if exposure to fluorescent lamps present in the BSLII cabinet could generate an energy, at the appropriate wavelength, sufficient to photosensitize hypericin and phthalocyanine, and cause the consequent generation of singlet oxygen, influencing the detected antiviral activity.

Statistical Analysis

Data are presented as average ± standard deviation (SD) of at least 3 independent experiments. Differences within each group were subjected to the t-test. Statistically significant differences (* $p \leq 0.05$, ** $p \leq 0.01$, *** $p \leq 0.001$, and **** $p \leq 0.001$) are indicated by the lines between the compared groups.

RESULTS

GaMD simulations of hypericin and phthalocyanine

Phthalocyanine and hypericin insertion in the membrane envelope

A complete model of the S protein inserted in a viral membrane (Woo et al., 2020), has been simulated in the presence and absence of several phthalocyanine (referred as S-PHT system) or hypericin (referred as S-HYP system) molecules randomly placed in the solvent. A system without these compounds has also been simulated as a reference (referred as S-REF system).

During the simulations one phthalocyanine and two hypericin molecules entered the viral membrane, with the phthalocyanine inserting after 35 ns while both hypericin molecules already in the first pre-GaMD equilibration phases. After their insertion, due to their size and chemical nature, these molecules remained located below the interface, between the hydrophobic lipid tails and the polar heads, although one hypericin deeply crosses the bilayer, almost reaching the leaflets interface (Figure 1). The binding location achieved by the two hypericin molecules is consistent with that of another simulation study (Gattuso et al., 2017). No preferential binding for the different lipid types composing the bilayer has been detected.

To evaluate the effects generated by the presence of these molecules on the viral envelope, we calculated membrane thickness heatmaps, describing the thickness profile along the membrane z-axis as illustrated by a colour scale. Average thickness values have been calculated over the production phase of the GaMD trajectory (50-150 ns) (Figure 1). This analysis highlighted distinct alterations in the thickness pattern between the three systems, particularly in the molecules' insertion regions. Compared with the reference system where wider regions of higher thickness are observed, both compounds induce a decrease in membrane thickness and a general re-organization of its pattern in the whole bilayer (Figure 1).

To obtain a more detailed description of thickness fluctuations during the simulations, we determined the abundance of thicker regions (thickness ≥ 44 Å) within the heatmaps calculated for the entire GaMD trajectory (Figure S1). Percentage of thicker regions, in comparison with the total number of points defining the membrane shape, is a quantitative indication of the differences observed in the three conditions. Results show that the reference membrane experiences a gradual increase in thickness during the entire simulation, with the percentage of thicker regions increasing from 10 to about 36% in the last part of the simulation (Figure S1A). On the other hand, in the S-PHT system the bilayer stably maintains a lower thickness profile, increasing and stabilizing at about 28% at the end of the simulation (Figure S1B). In the S-HYP system, an even lower abundance of thicker regions is detected in the first 50-60 ns, which then slightly increases and fluctuates around 20-29% until the end of the simulation (Figure S1C). In both cases, the percentage of these regions is generally lower than that calculated for the reference membrane (Figure S1A).

These results suggest that a possible inhibition mechanism mediated by these two compounds could involve an alteration of the physical properties and structural organization of the viral envelope. Indeed, non-specific binding of viral membranes has already been hypothesized to contribute to hypericin antiviral activity against enveloped viruses (Weber et al., 1994). Since membrane biophysical properties are crucial to maintain and complete viral and cell membrane fusion, the insertion of these compounds could decrease the overall efficiency of the viral fusion process.

Phthalocyanine and hypericin interactions with the S protein

To obtain an overview of phthalocyanine and hypericin molecules distribution around the protein surface, radial distribution functions (RDFs), describing how molecules densities change as a function of distance from the protein surface, were calculated and averaged for the entire trajectory (Figure S2). The analysis highlighted that hypericin molecules are strongly attracted toward the S surface, arranging close to the structure and forming one density peak between 1.0 - 2.0 nm from the protein. On the other hand, phthalocyanines are less gathered around the S and show less than half hypericin density at short distances. These results indicate that phthalocyanines mostly fluctuate in the solvent without specifically or persistently interacting with the protein surface during the simulation. Indeed, contact analysis showed that only six phthalocyanine molecules closely interact with the S for more than 50% of the simulation time: three phthalocyanine molecules bind to its NTDs for about 73, 56 and 83% of simulation time, respectively, while one molecule binds the fusion peptide region for 49% of the simulation and another binds the HR2 regions for 71% of simulation time. Other phthalocyanine compounds establish only short and transient contacts with the RBDs (7 and 3%) at the end of the trajectory or with the HR1 domain (4%).

On the contrary, several hypericin molecules stably contact critical S regions. In particular, each RBD is bound by a hypericin molecule for 99, 78 and 48% of the simulation time, respectively (Figure 2A). Two of these compounds specifically contact the RBM, involved in ACE2 binding, and one of them is inserted into a pocket at the interface of the three RBDs. This allows to hypothesize that the binding of these molecules could limit the motion of these regions, causing a decrease in the frequency of RBDs transitions to the open conformation and a consequent reduction of S interactions with the ACE2 receptor. Another hypericin binds to a distal region of one RBD for 79% of the simulation time (Figure 2A). Several hypericin molecules also bind to the protein NTDs, with persistence ranging from 87 to 33%. Two hypericin molecules localize around the S HR1 domains, binding at the interface of a cavity facing the protein internal pocket and, particularly, to the fusion peptide regions for 76 and 67% of the simulation time, respectively (Figure 2B).

An group of aggregated hypericin molecules also contacts the HR2 domains from 99 to 26% of the simulation time (Figure 2C). Interactions of molecules with these domains could likely affect the final assembly of the HR1 and HR2 into the pore-inducing six-helix bundle (6-HB), blocking their interactions and interfering with fusion peptide cleavage and release, ultimately hindering S transition to postfusion conformation.

Influence of phthalocyanine and hypericin on protein's correlated motions

Principal component analysis (PCA) (Amadei et al., 1993) has been performed on S Cα atoms to evaluate if the interaction with phthalocyanine or hypericin could influence the protein structural dynamics. Through this technique, it is possible to isolate the major fluctuations contributing to the protein structural dynamics by identifying the principal 3N directions along which most of the protein motion is described. Cross-correlation matrices were generated for both systems, where a positive correlation indicates that the residues move in the same direction, a negative correlation identifies residues moving in opposite directions, while a null correlation indicates residues having uncorrelated motions. To highlight relevant differences in the three simulated conditions, cross-correlation matrices obtained for the S Cα in the three simulations have been subtracted, obtaining three differences matrices (Figure S3). This way, only residues couples showing an altered behaviour in the two compared conditions are highlighted, while protein regions showing a similar dynamical behaviour are shown in white. Although the type of correlated motion (positive or negative) identified between each residue couple cannot anymore be distinguished after subtraction of the matrices, the obtained plots show that the presence of phthalocyanine or hypericin induces a different dynamical behaviour in several protein regions in comparison with the S-REF (Figure S3). Protein regions showing the highest differences can be distinguished by small areas containing highly clustered

coloured points. Concerning hypericin, this effect is particularly evident in the protein NTDs and RBDs, the regions mostly contacted by this compound (Figure S3B). On the other hand, the S-PHT/S-HYP correlation differences highlight that S motions alterations observed in the presence of the two compounds are similar and only show minor differences in their pattern or intensity in all main considered protein domains (Figure S3C). Interestingly, in the presence of these molecules, altered motions in the protein CTD can be observed (Figure S3A, B), suggesting that the variations in membrane thickness observed in the S-PHT and S-HYP simulations (Figure 1) could also have influenced the dynamics of protein regions in direct contact with the bilayer.

The first eigenvector calculated from the covariance matrices accounts for about 46% of the total protein motion and has been selected for further analysis. Indeed, analysis of the direction and amplitude of this eigenvector and its individual vector components (x, y and z) confirmed that the S backbone atoms undergo different oscillations in the 3D space during the simulations. To highlight the regions showing the highest deviations, differences have been calculated between the total and individual eigenvectors of the S-REF/S-PHT (Figure S4A) or S-REF/S-HYP (Figure S4B) systems. Although higher deviations in eigenvectors amplitudes are observed in the CTD regions of the protein monomer A or B of the S-PHT or S-HYP systems, respectively, the two difference plots display a similar trend of variability in all three protein monomers, suggesting that protein motions are similarly altered by the two compounds, in comparison with the S-REF. Indeed, projection of the trajectory on the first eigenvector over the simulation time revealed that directions of the main motion characterizing the S protein are very similar in the S-PHT and S-HYP simulations, while they show an opposite fluctuation in the S-REF (Figure S4C). This suggests that ligands interactions with the protein, whether stable or more transient, and their diffusion around the protein surface, could alter the major motions defining the S protein dynamics, and should consequently influence its native conformational behaviour on the virion surface.

Salt bridges patterns

Interestingly, in the presence of compounds we observed a slight increase in the total number of salt bridges stabilizing the protein during the simulations (127, 132 and 138 for the S-REF, S-HYP and S-PHT systems, respectively). Salt bridges absence or presence can strongly affect the overall protein function since they contribute to constraining protein motion and influencing its flexibility and conformation (Kumar & Nussinov, 2002). The analysis was further restricted to the S CTDs, showing that the pattern of salt bridges established in this domain is substantially altered in the three systems, particularly in the S-HYP simulation (Table S1). In detail, in the S-REF CTD only two highly persistent (E1258.C - K1269.C: 79 %, D1259.B - K1269.B: 75%) and two moderately persistent

(E1262.A - K1266.A: 39%, E1258.A - K1269.A: 25%) salt bridges were identified (Table S1). On the other hand, in the S-HYP system no high-persistence salt bridges were detected (> 70%). Nevertheless, 9 salt bridges with persistence ranging from 15 to 54% and two with persistence ≤ 10% of the simulation time were observed. Similarly, in the S-PHT simulation, 6 salt bridges with persistence ranging from 12 to 53% and 1 with persistence of only about 3% were identified (Table S1). The higher number of S CTD salt bridges with larger instability detected in the presence of compounds further confirms that the protein experiences an altered flexibility during the simulations, additionally supporting the hypothesis that the membrane thickness alterations observed affect the S protein domains' behaviour.

Microseconds CG-MD simulations of hypericin interactions with a SARS-CoV-2 S glycoprotein and membrane envelope model

To extend the observation timescale, an equivalent SARS-CoV-2 envelope portion model was also simulated at CG resolution, selecting only hypericin as an inhibitory molecule, since this compound was identified as the prominent protein-membrane interactor in the atomistic trajectory. 14 CG-MD simulation replicas have been performed for the system with hypericins (CG-HYP) and 5 replicas for a reference system without hypericins (CG-REF). All systems and replicas have been simulated for 10.0 μs.

Due to its amphipathic character, hypericin is highly attracted to the membrane, with about 6 to 14 hypericin molecules inserted in the bilayer during each simulation. Therefore, as opposed to what was observed in the GaMD simulation, most of these molecules were bound to the membrane and not in contact with the protein. Although membrane thickness showed no evident changes, evaluating 41 Å on average in both simulated conditions, thicker regions (> 45 Å) were more frequently observed in the CG-HYP system, particularly during the first 5 μs (Figure S5). However, percentage of maps points identifying these regions is similar in the two conditions. Since a lower average membrane thickness has been observed in the CG membrane model, the high-thickness threshold has been decreased from the 44 Å applied for the GaMD simulations to 42 Å, and percentages have been calculated every 1 μs. Calculations showed very similar values in the two conditions, with a percentage of high thickness points ranging from 3 to 11% in the CG-REF system and from 2 to 12% in the CG-HYP system.

Interaction analysis highlighted hypericin molecules attachment to particular functional regions of the S protein. On average, in the 14 replicas, 1 to 4 molecules were bound to the NTD, 0 to 4 molecules to the RBD, 3 to 8 molecules to the whole protein “head” region, 0 to 2 molecules to the HR1 domain, 0 to 3 molecules to the fusion peptide segment, 1 to 4 molecules to the protein “stalk” and 1 to 2

molecules to the CTD. Aggregation of hypericin molecules at the protein HR2 domain was not observed in the CG simulations, probably because of the higher curvature and fluctuations experienced by this region in the longer simulated timescale.

An overview of hypericin molecules distribution over the S surface was obtained by generating volumetric maps around the protein ectodomain (Figure 3). Maps were generated for each simulation replica using the *volmap* tool of VMD (Humphrey et al., 1996), which allowed to calculate the occupancy of each hypericin over the protein surface, mapping the obtained values as grid surfaces on the protein 3D structure. In this case, hypericin grids positions indicate main binding locations achieved by the compounds during the simulations. As shown in Figure 3, hypericin compounds mostly cluster around the protein NTDs, RBDs and HR1 domains. In particular, binding locations achieved on the RBD are similar to those observed in the atomistic GaMD simulation (Figure 2A and 3B), with some hypericin molecules located among the interface of the three RBDs (Figure 3B, upper image), and others at a more distal region of the domain (Figure 3B, lower image). Similarly, in both atomistic and CG simulations, the binding of hypericin molecules around the HR1 domains involves their interaction with the fusion peptides (Figure 2B and 3C), and remarkable replicability of hypericin binding sites on these regions can be observed for the three S monomers (Figure S6). The overall reproducibility of hypericin binding locations in the different simulation replicas and in both all-atom and coarse-grained resolutions, strongly indicates that these regions possess specific surface crevices favouring the recognition and the attachment of free solvated hypericin molecules.

Interestingly, in four replicas we also observed the insertion of two to three hypericin molecules at the interface of the S internal cavity (Figure 3 and 4A-D). This evidence strongly supports the inhibition mechanism hypothesized in our previous paper (Romeo et al., 2020), suggesting that the steric hindrance generated by molecules' aggregation at this interface could hinder S transition to postfusion conformation and prevent the correct initiation of the virus-cell membrane fusion process.

Since S bending is crucial for correctly approaching the ACE2 receptor, protein bending angles were also monitored in both conditions to evaluate if compounds attachment could alter S motion and, possibly, its efficiency in attaching the cell receptor. Bending angles were calculated between the centers of mass of the initial, central and terminal regions of the protein "stalk" (residues 1143-1153, 1167-1173 and 1190-1194) (Figure S7A). Similar results have been obtained for the S protein in the CG-REF and CG-HYP systems (Figure S7B). A slightly higher bending is achieved towards the end of the first CG-REF replica, with an angle value of about 84°. On the other hand, 94° was the lowest value observed for the hypericin-bound protein. 8 of the 15 CG-HYP replicas display a stable decrease in their bending angle during the 10 μs (Figure S7B). The same is observed in 2 out of 5 CG-REF replicas (Figure S7B). The achieved protein curvatures are overall maintained until the end

of the simulation and the transition to a higher bending is observed between 2.5 to 9.0 μs in the different replicas, in both conditions (Figure S7B).

Inspecting the last frames of each replica, both in the absence or presence of hypericin, the S achieves three conformations characterized by low, moderate, or high curvature (Figure S8A-C). In the high curvature conformation, the protein directly contacts the membrane with its NTDs and/or part of its RBDs and, in some replicas, this binding also involves the simultaneous interaction of the protein with one or more hypericin molecules inserted in the membrane (Figure S8C). This interaction can be explained by the strong positive potential characterizing the S NTDs, which are attracted by the negative potential surface of the membrane (Figure S8D). On the other hand, the protein "stalk" region is mostly characterized by a negative electrostatic potential (Figure S8D). A possible function of this negative potential region could be to limit S bending towards the negatively charged plane of the membrane, which is observed only after several μs of simulation, a hypothesis already proposed for the lectin-like oxidized low-density lipoprotein receptor-1 (LOX-1) which shows a similar electrostatic potential distribution (Biocca et al., 2013). Although S proteins can be highly tilted towards the envelope membrane, up to 90° relative to the bilayer as experimentally observed (Ke et al., 2020), it is unlikely that these glycoproteins would achieve such a dramatic bending on the envelope and stably attach the nearby viral membrane surface, and thus this effect could represent an artefact due to the CG model approximations.

In vitro antiviral activity of phthalocyanine and hypericin

Experimental tests have been carried out to validate the efficacy of phthalocyanine and hypericin in blocking virus entry. The potential antiviral activity of these compounds has been tested in an *in vitro* model of infection of HEK293T/ACE2 cellular line with SARS-CoV-2 Pseudotyped Luciferase Lentivirus (i.e., a harmless virus expressing the SARS-CoV-2 S protein). First, a series of preliminary experiments has been performed to establish the best culture and infection conditions (Figure S9). Different multiplicities of infections (MOI 5:1/ 10:1 / 20:1 / 50:1) have been used to establish which virus:cell ratio guaranteed the maximum efficacy of infection and the minimum cell mortality. According to the results, all subsequent experiments have been performed at MOI 10:1 virus-cells. To evaluate suitable non-toxic doses for antiviral testing, different serial compounds concentrations (ranging from 12.50 μg/ml to 0.005 μg/ml) and time of incubation were tested on HEK293T/ACE2 cells (cells transfected with ACE2), using the MTT-based cytotoxicity test. No toxicity has been revealed at the highest compound concentrations and treatment time used (Figure S9). At this point, a first set of infection assays was carried out using serial concentration of the compounds (from 0.005 μg/ml to 0.78 μg/ml), showing that both hypericin and phthalocyanine start to inhibit the pseudo-

typed virus already at the lowest concentration of 0.005 μg/ml. Therefore, we selected only the extreme concentrations in the evaluated range (C1: 0.78 μg/ml and C2: 0.005 μg/ml) to conduct subsequent experiments and to obtain a statistically significant validation of the observed antiviral effect.

According to the photosensitizer properties of both hypericin and phthalocyanine, these compounds could produce toxic oxygen and radical species in the presence of light during the evaluated experimental conditions. Therefore, we performed a series of parallel experiments in dark (light off) and normal conditions (e.g., under BSLII cabinet, with the light switched on at an intensity of 1187.1 Lux) to investigate ROS production induced by hypericin or phthalocyanine in our experimental model. As shown in Figure 5A, hypericin or phthalocyanine treatment at the two selected concentrations does not induce ROS production in HEK293T/ ACE2 cells, under either condition. These results allow to exclude any cellular oxidative stress interference of the treatment on cellular viability or metabolism.

The anti-SARS-CoV-2 activity of hypericin and phthalocyanine was tested using a Pseudotyped (PSV) Luciferase Lentivirus system expressing the SARS-CoV-2 S protein on its surface, which allowed to analyse SARS-CoV-2 attachment and entry into ACE2-expressing cells. Three different treatment conditions have been applied to test the possible entry inhibition mediated by hypericin or phthalocyanine and to evaluate their putative mode of action against SARS-CoV-2:

I. pre-treatment of the pseudovirus with the two compounds for 2 h, before infection;
II. pre-treatment of the HEK293T/ACE2 cells with the two compounds for 2 h, before infection;
III. simultaneous addition of the two compounds and pseudovirus to cells.

Pseudovirus infected cells (no treatment) have been used as a positive control, while untreated and uninfected cells have been included as negative controls. In both cases, two different concentrations of compounds (C1: 0.78 μg/ml; C2: 0.005 μg/ml) have been used for the experiments. The obtained results represent an average of three different series of experiments. As shown in Figure 5B, only the pseudovirus pre-treatment with hypericin or phthalocyanine, prior to cells infection (condition I), resulted in a robust reduction of virus entry into cells (****P <0.0001), with small and non-statistically significant differences observed between the two concentrations tested. In this condition hypericin reduced the number of infected cells by 97% at C1 and 95% at C2, while a reduction of 96% at both C1 and C2 was induced by phthalocyanine, compared to the positive control (non-treated only infected cells). Pre-treatment of HEK293T/ACE2 with the compounds for 2 hours, followed by infection, did not influence viral entry (condition II). Moreover, experiments carried out in condition III, in which the cells have been simultaneously treated with hypericin or phthalocyanine and infected

with the pseudovirus, only resulted in a slight non-statistically significant reduction in infected cells treated at higher concentrations (Figure 5B).

These data demonstrate that both compounds exert a strong antiviral action on SARS-CoV-2 when in contact with the virus before cell infection, while they exert no direct effect on the cells. This suggests that their activity should involve the targeting of viral envelope surface components (i.e., the S glycoprotein and/or its lipid envelope), as also suggested by the computational results.

DISCUSSION

Computational and *in vitro* results described in this work allowed to evaluate the possible role of hypericin and phthalocyanine, top-ranking compounds retrieved from a previously performed virtual screening (Romeo et al., 2020), as effective SARS-CoV-2 entry inhibitors.

The all-atom and CG simulations allowed to delineate the potential antiviral activity of phthalocyanine and hypericin at different atomistic resolutions. In particular, all-atom GaMD simulations of a complete model of the SARS-CoV-2 S glycoprotein, embedded in a membrane mimicking the viral envelope, allowed to highlight the presence of several drugs' binding sites on the protein surface and to verify their propensity to insert in membranes. Simulations showed that the two compounds insert within the viral membrane (Figure 1), modifying its thickness profile and possibly leading to an overall alteration in the envelope structural organization which could influence viral and cell membrane fusion (Figure 1, S1). Indeed, hypericin has been reported to inactivate a wide variety of enveloped viruses, while it is inactive against naked viruses, supporting the hypothesis that its antiviral activity might be dependent on the presence of an outer lipid membrane (Kubin et al., 2005; Weber et al., 1994).

Phthalocyanine and hypericin can also interact with different S functional domains. Notably, hypericin molecules show a higher attraction than phthalocyanines towards both the membrane and the S protein (Figure S2), with several hypericin molecules specifically targeting key structural regions of S such as its RBD domains, two cavities close to the HR1 domains, and the HR2 domains (Figure 2). Since these regions are crucial in the process of viral attachment and fusion to the host cell, it can be hypothesized that hypericin may interfere through different mechanisms with the specific sequence of events leading to the final virus entry into cells (i.e., ACE2 receptor recognition, S conformational changes, HR1 and HR2 assembly into the postfusion 6-HB, membrane fusion) (Tang et al., 2020). Moreover, structural analysis on the S protein highlighted that the overall pattern of protein-correlated motions and the number and types of salt bridges established within its domains significantly changes in the presence of compounds (Figure S3, S4; Table S1), suggesting they could also affect the protein conformational dynamics and, consequently, its function. Notably, these effects

were also observed in the CTD, in direct contact with the membrane, proposing that the alterations observed in the bilayer can further influence the protein's dynamical behaviour.

Although GaMD simulations allowed to characterise compounds' interactions with the outer region of the virus, the main drawback of this model is the limited timescale of the simulation and the lack of replicas due to the system size and the highly demanding computational costs. To overcome this limitation, a similar system has been developed at CG resolution in the absence or presence of hypericin, the compound showing the highest affinity for the protein and membrane envelope components. The CG technique allowed to reduce the computational cost of simulations and to extend the sampling of about three orders of magnitude, from hundreds of ns to tenths of μs. CG simulations correctly reproduced published microsecond atomistic data (Casalino et al., 2020; Choi et al., 2021), confirming the reliability of this technique in increasing the observation timescales of biological processes.

Even starting from different initial configurations, hypericin achieved similar binding locations on the S surface, mainly contacting protein regions involved in virus attachment and fusion, similar to what was observed in the GaMD trajectory (the RBDs, internal cavity, fusion peptides and HR1 domains) (Figure 3, S6). In particular, the insertion of several hypericin molecules at the interface of the protein internal cavity (Figure 4) suggests that this compound could approach this interior region and prevent S transition to postfusion conformation, as suggested in our previous study (Romeo et al., 2020). Despite the several identified binding sites, in the presence of hypericin no significant differences in S protein curvature or orientation on the envelope surface have been observed (Figure S7 and S8). As opposed to the GaMD trajectories, several hypericin molecules inserted in the bilayer during CG simulations, although only small differences in membrane structural parameters could be identified in the two conditions (Figure S5). Data obtained through CG simulations support the hypothesis that hypericin antiviral activity could mostly rely on its binding to different protein regions and on its insertion within the viral membrane. This would allow this compound to interfere with virus-host cell interactions and possibly also to exert its photosensitizing activity, as already observed against other enveloped viruses (Kubin et al., 2005; Smetana et al., 1994).

Following the obtained computational results, experimental data obtained with a SARS-CoV-2 pseudovirus expressing the S protein suggest that pre-treatment of the virus with low concentrations of these two compounds (0.78 μg/ml and 0.005 μg/ml) strongly inhibits its cell entry (Figure 5B). On the other hand, no effect was recorded with the addition of compounds at the moment of infection. This behaviour indicates that the detected antiviral activity should involve the targeting of the viral envelope surface, as indicated by the computational data, and that the compounds fail to limit the paroxysmal phenomenon of S conformational transition when this event is already triggered.

Other published works also sustain our results, showing that hypericin and *H. perforatum* extracts can inhibit SARS-CoV-2 activity *in vitro* with no cytotoxic effects (Bajrai et al., 2022; Delcanale et al., 2022; Jang et al., 2021; Matos et al., 2022; Mohamed et al., 2022), and that a phthalocyanine-containing mouthwash could be effective in treating hospitalized COVID-19 patients (da Silva Santos et al., 2021). Considering the computational and experimental results obtained, and also literature evidences, it can be hypothesized that the antiviral activity of these compounds on the viral envelope surface could be mediated by a combination of two mechanisms: on the one hand, through the binding and perturbation of the surface proteins and viral membrane structural and dynamical properties, as observed in our simulations; on the other, through the production of activated oxygen molecules as reported in literature (Kubin et al., 2005). However, our data suggest that hypericin and phthalocyanine treatment does not induce ROS production at the concentrations and conditions evaluated (Figure 5A), allowing to exclude a role of oxidative stress in the anti-SARS-CoV-2 activity mediated by these compounds and further supporting the antiviral mechanism suggested by the computational analyses. Notably, hypericin has also been reported as a potent inhibitor of the Cathepsin L protease, which plays an important role in SARS-CoV-2 entry through the endosomal route by activating the S glycoprotein in the endosomes or lysosomes (Pan et al., 2022), further promoting the applicability of this compound as a multimodal entry inhibitor.

The marked antiviral activity detected in our experiments is observed in the absence of direct irradiation and without the production of ROS, unlike what has mostly been observed for other enveloped viruses (Korneev et al., 2019; Kubin et al., 2005; Lenard et al., 1993), suggesting that these compounds may have a specificity towards the SARS-CoV-2 S glycoprotein which allows for a direct inhibition of its binding and fusion to the host cell. As suggested in our previous virtual screening, this effect may also rely on the specific binding of compounds within an internal cavity of the prefusion protein (Romeo et al., 2020).

In conclusion, the obtained *in silico* and *in vitro* results endorse the hypothesis of a further evaluation of phthalocyanine and hypericin as antiviral compounds against SARS-CoV-2 and, possibly, other viruses sharing similar envelope components.

Acknowledgments

The authors thank Prof. S.J. Marrink, Dr. T.A. Wassenaar and the MD group of the University of Groningen for hosting part of this research and for their help in implementing the CG systems.

The computing resources and the related technical support used for this work have been provided by CRESCO/ENEAGRID High Performance Computing infrastructure and its staff (Iannone et al., 2019). CRESCO/ENEAGRID High Performance Computing infrastructure is funded by ENEA, the

673 Italian National Agency for New Technologies, Energy and Sustainable Economic Development and
674 by Italian and European research programmes, see http://www.cresco.enea.it/english for information.
675

676 **Funding**
677 This work was supported by the "National Research Center in High Performance Computing, Big
678 Data and Quantum Computing", as part of the National Recovery and Resilience Plan (PNRR) -
679 Mission 4 Component 2, "From research to business" Investment 1.4, "Strengthening of research
680 structures and creation of "national R&D champions" on certain Key Enabling Technologies". MUR
681 identification code: CN_00000013.
682

683 **Author contributions**
684 A.R. and G.C.: Methodology, Formal analysis, Investigation, Writing-Original Draft, Writing-
685 Review and Editing; F.I.: Methodology, Investigation, Writing-Review and Editing; V.C.: Writing-
686 Review and Editing, Supervision; M.F.: Conceptualization, Methodology, Formal analysis, Data
687 Curation, Writing-Original Draft, Writing-Review and Editing, Supervision.
688

689 **Disclosure statement**
690 The authors report there are no competing interests to declare.
691

692 **Data availability statement**
693 Data will be made available on request.
694

REFERENCES

Abraham, M. J., Murtola, T., Schulz, R., Páll, S., Smith, J. C., Hess, B., & Lindah, E. (2015). Gromacs: High performance molecular simulations through multi-level parallelism from laptops to supercomputers. *SoftwareX*, *1–2*, 19–25. https://doi.org/10.1016/j.softx.2015.06.001

Amadei, A., Linssen, A. B. M., & Berendsen, H. J. C. (1993). Essential dynamics of proteins. *Proteins: Structure, Function, and Genetics*, *17*(4), 412–425. https://doi.org/10.1002/prot.340170408

Bajrai, L. H., Ali, S., Kafrawy, E., Hassan, A. M., Tolah, A. M., Alnahas, R. S., Sohrab, S. S., Rehan, M., & Azhar, E. I. (2022). In vitro screening of anti - viral and virucidal effects against SARS - CoV - 2 by Hypericum perforatum and Echinacea. *Scientific Reports*, 1–17. https://doi.org/10.1038/s41598-022-26157-3

Battles, M. B., Langedijk, J. P., Furmanova-Hollenstein, P., Chaiwatpongsakorn, S., Costello, H. M., Kwanten, L., Vranckx, L., Vink, P., Jaensch, S., Jonckers, T. H. M., Koul, A., Arnoult, E., Peeples, M. E., Roymans, D., & McLellan, J. S. (2016). Molecular mechanism of respiratory syncytial virus fusion inhibitors. *Nature Chemical Biology*, *12*(2), 87–93. https://doi.org/10.1038/nchembio.1982

Battles, M. B., & McLellan, J. S. (2019). Respiratory syncytial virus entry and how to block it. *Nature Reviews Microbiology*, *17*(4), 233–245. https://doi.org/10.1038/s41579-019-0149-x

Biocca, S., Arcangeli, T., Tagliaferri, E., Testa, B., Vindigni, G., Oteri, F., Giorgi, A., Iacovelli, F., Novelli, G., Desideri, A., & Falconi, M. (2013). Simulative and experimental investigation on the cleavage site that generates the soluble human LOX-1. *Archives of Biochemistry and Biophysics*, *540*(1–2), 9–18. https://doi.org/10.1016/j.abb.2013.10.001

Bussi, G., Donadio, D., & Parrinello, M. (2007). Canonical sampling through velocity rescaling. *Journal of Chemical Physics*, *126*(1). https://doi.org/10.1063/1.2408420

Casalino, L., Gaieb, Z., Goldsmith, J. A., Hjorth, C. K., Dommer, A. C., Harbison, A. M., Fogarty, C. A., Barros, E. P., Taylor, B. C., Mclellan, J. S., Fadda, E., & Amaro, R. E. (2020). Beyond shielding: The roles of glycans in the SARS-CoV-2 spike protein. *ACS Central Science*, *6*(10), 1722–1734. https://doi.org/10.1021/acscentsci.0c01056

Chen, H., Feng, R., Muhammad, I., Abbas, G., Zhang, Y., Ren, Y., Huang, X., Zhang, R., Diao, L., Wang, X., & Li, G. (2019). Protective effects of hypericin against infectious bronchitis virus induced apoptosis and reactive oxygen species in chicken embryo kidney cells. *Poultry Science*, *98*(12), 6367–6377. https://doi.org/10.3382/ps/pez465

Chen, H., Muhammad, I., Zhang, Y., Ren, Y., Zhang, R., Huang, X., Diao, L., Liu, H., Li, X., Sun, X., Abbas, G., & Li, G. (2019). Antiviral Activity Against Infectious Bronchitis Virus and Bioactive Components of Hypericum perforatum L. *Frontiers in Pharmacology*, *10*, 1272. https://doi.org/10.3389/fphar.2019.01272

Choi, Y. K., Cao, Y., Frank, M., Woo, H., Park, S. J., Yeom, M. S., Croll, T. I., Seok, C., & Im, W. (2021). Structure, Dynamics, Receptor Binding, and Antibody Binding of the Fully Glycosylated Full-Length SARS-CoV-2 Spike Protein in a Viral Membrane. *Journal of Chemical Theory and Computation*, *17*(4), 2479–2487. https://doi.org/10.1021/acs.jctc.0c01144

da Silva Santos, P. S., da Fonseca Orcina, B., Machado, R. R. G., Vilhena, F. V., da Costa Alves, L. M., Zangrando, M. S. R., de Oliveira, R. C., Soares, M. Q. S., Simão, A. N. C., Pietro, E. C. I. N., Kuroda, J. P. G., de Almeida Benjamim, I. A., Araujo, D. B., Toma, S. H., Flor, L., Araki, K., & Durigon, E. L. (2021). Beneficial effects of a mouthwash containing an antiviral phthalocyanine derivative on the length of hospital stay for COVID-19: randomised trial. *Scientific Reports*, *11*(1), 19937. https://doi.org/10.1038/s41598-021-99013-5

Darden, T., York, D., & Pedersen, L. (1993). Particle mesh Ewald: An N ·log(N) method for Ewald sums in large systems. *The Journal of Chemical Physics*, *98*(12), 10089–10092. https://doi.org/10.1063/1.464397

Degar, S., Prince, A. M., Pascual, D., Lavie, G., Levin, B., Mazur, Y., Lavie, D., Ehrlich, L. S., Carter, C., & Meruelo, D. (1992). Inactivation of the Human Immunodeficiency Virus by Hypericin: Evidence for Photochemical Alterations of p24 and a Block in Uncoating. *AIDS Research and Human Retroviruses*, *8*(11), 1929–1936. https://doi.org/10.1089/aid.1992.8.1929

Delcanale, P., Uriati, E., Mariangeli, M., Mussini, A., Moreno, A., Lelli, D., Cavanna, L., Bianchini, P., Diaspro, A., Abbruzzetti, S., & Viappiani, C. (2022). The Interaction of Hypericin with SARS-CoV-2 Reveals a Multimodal Antiviral Activity. *ACS Applied Materials and Interfaces*, *14*(12), 14025–14032. https://doi.org/10.1021/acsami.1c22439

Feller, S. E., Zhang, Y., Pastor, R. W., & Brooks, B. R. (1995). Constant pressure molecular dynamics simulation: The Langevin piston method. *The Journal of Chemical Physics*, *103*(11), 4613–4621. https://doi.org/10.1063/1.470648

François, K. O., Pannecouque, C., Auwerx, J., Lozano, V., Pérez-Pérez, M. J., Schols, D., & Balzarini, J. (2009). The phthalocyanine prototype derivative Alcian blue is the first synthetic agent with selective anti-human immunodeficiency virus activity due to its gp120 glycan-binding potential. *Antimicrobial Agents and Chemotherapy*, *53*(11), 4852–4859. https://doi.org/10.1128/AAC.00811-09

Gattuso, H., Marazzi, M., Dehez, F., & Monari, A. (2017). Deciphering the photosensitization mechanisms of hypericin towards biological membranes. *Physical Chemistry Chemical Physics*, *19*(34), 23187–23193. https://doi.org/10.1039/c7cp03723f

Goga, N., Rzepiela, A. J., De Vries, A. H., Marrink, S. J., & Berendsen, H. J. C. (2012). Efficient algorithms for langevin and DPD dynamics. *Journal of Chemical Theory and Computation*, *8*(10), 3637–3649. https://doi.org/10.1021/ct3000876

Greco, E., Quintiliani, G., Santucci, M. B., Serafino, A., Ciccaglione, A. R., Marcantonio, C., Papi, M., Maulucci, G., Delogu, G., Martino, A., Goletti, D., Sarmati, L., Andreoni, M., Altieri, A., Alma, M., Caccamo, N., Di Liberto, D., De Spirito, M., Savage, N. D., … Fraziano, M. (2012). Janus-faced liposomes enhance antimicrobial innate immune response in Mycobacterium tuberculosis infection. *Proceedings of the National Academy of Sciences*, *109*(21). https://doi.org/10.1073/pnas.1200484109

Grünewald, F., Kroon, P. C., Souza, P. C. T., & Marrink, S. J. (2021). Protocol for Simulations of PEGylated Proteins with Martini 3. *Methods in Molecular Biology*, *2199*, 315–335. https://doi.org/10.1007/978-1-0716-0892-0_18

Guixà-González, R., Rodriguez-Espigares, I., Ramírez-Anguita, J. M., Carrió-Gaspar, P., Martinez-Seara, H., Giorgino, T., & Selent, J. (2014). MEMBPLUGIN: studying membrane complexity in VMD. *Bioinformatics*, *30*(10), 1478–1480. https://doi.org/10.1093/bioinformatics/btu037

Guvench, O., Mallajosyula, S. S., Raman, E. P., Hatcher, E., Vanommeslaeghe, K., Foster, T. J., Jamison, F. W., & MacKerell, A. D. (2011). CHARMM Additive All-Atom Force Field for Carbohydrate Derivatives and Its Utility in Polysaccharide and Carbohydrate–Protein Modeling. *Journal of Chemical Theory and Computation*, *7*(10), 3162–3180. https://doi.org/10.1021/ct200328p

Hess, B., Bekker, H., Berendsen, H. J. C., & Fraaije, J. G. E. M. (1997). LINCS: A Linear Constraint Solver for molecular simulations. *Journal of Computational Chemistry*, *18*(12), 1463–1472. https://doi.org/10.1002/(SICI)1096-987X(199709)18:12<1463::AID-JCC4>3.0.CO;2-H

Huang, J., Rauscher, S., Nawrocki, G., Ran, T., Feig, M., De Groot, B. L., Grubmüller, H., & MacKerell, A. D. (2016). CHARMM36m: An improved force field for folded and intrinsically disordered proteins. *Nature Methods*, *14*(1), 71–73. https://doi.org/10.1038/nmeth.4067

Hudson, J. B., Harris, L., & Towers, G. H. N. (1993). The importance of light in the anti-HIV effect of hypericin. *Antiviral*

Research, *20*(2), 173–178. https://doi.org/10.1016/0166-3542(93)90006-5

Humphrey, W., Dalke, A., & Schulten, K. (1996). VMD: Visual molecular dynamics. *Journal of Molecular Graphics*, *14*(1), 33–38. https://doi.org/10.1016/0263-7855(96)00018-5

Iannone, F., Ambrosino, F., Bracco, G., De Rosa, M., Funel, A., Guarnieri, G., Migliori, S., Palombi, F., Ponti, G., Santomauro, G., & Procacci, P. (2019). CRESCO ENEA HPC clusters: A working example of a multifabric GPFS Spectrum Scale layout. *2019 International Conference on High Performance Computing and Simulation, HPCS 2019*, 1051–1052. https://doi.org/10.1109/HPCS48598.2019.9188135

Jang, W. D., Jeon, S., Kim, S., & Lee, S. Y. (2021). Drugs repurposed for COVID-19 by virtual screening of 6,218 drugs and cell-based assay. *Proceedings of the National Academy of Sciences*, *118*(30), e2024302118. https://doi.org/10.1073/pnas.2024302118

Jo, S., Kim, T., Iyer, V. G., & Im, W. (2008). CHARMM-GUI: A web-based graphical user interface for CHARMM. *Journal of Computational Chemistry*, *29*(11), 1859–1865. https://doi.org/10.1002/jcc.20945

Jorgensen, W. L., Chandrasekhar, J., Madura, J. D., Impey, R. W., & Klein, M. L. (1983). Comparison of simple potential functions for simulating liquid water. *The Journal of Chemical Physics*, *79*(2), 926–935. https://doi.org/10.1063/1.445869

Karioti, A., & Bilia, A. R. (2010). Hypericins as Potential Leads for New Therapeutics. *International Journal of Molecular Sciences*, *11*(2), 562–594. https://doi.org/10.3390/ijms11020562

Ke, Z., Oton, J., Qu, K., Cortese, M., Zila, V., McKeane, L., Nakane, T., Zivanov, J., Neufeldt, C. J., Cerikan, B., Lu, J. M., Peukes, J., Xiong, X., Kräusslich, H. G., Scheres, S. H. W., Bartenschlager, R., & Briggs, J. A. G. (2020). Structures and distributions of SARS-CoV-2 spike proteins on intact virions. *Nature*, *588*(7838), 498–502. https://doi.org/10.1038/s41586-020-2665-2

Kim, S., Chen, J., Cheng, T., Gindulyte, A., He, J., He, S., Li, Q., Shoemaker, B. A., Thiessen, P. A., Yu, B., Zaslavsky, L., Zhang, J., & Bolton, E. E. (2021). PubChem in 2021: new data content and improved web interfaces. *Nucleic Acids Research*, *49*(D1), D1388–D1395. https://doi.org/10.1093/nar/gkaa971

Klauda, J. B., Venable, R. M., Freites, J. A., O'Connor, J. W., Tobias, D. J., Mondragon-Ramirez, C., Vorobyov, I., MacKerell, A. D., & Pastor, R. W. (2010). Update of the CHARMM All-Atom Additive Force Field for Lipids: Validation on Six Lipid Types. *The Journal of Physical Chemistry B*, *114*(23), 7830–7843. https://doi.org/10.1021/jp101759q

Korneev, D., Kurskaya, O., Sharshov, K., Eastwood, J., & Strakhovskaya, M. (2019). Ultrastructural aspects of photodynamic inactivation of highly pathogenic avian H5N8 influenza virus. *Viruses*, *11*(10), 955. https://doi.org/10.3390/v11100955

Kubin, A., Wierrani, F., Burner, U., Alth, G., & Grunberger, W. (2005). Hypericin - The Facts About a Controversial Agent. *Current Pharmaceutical Design*, *11*(2), 233–253. https://doi.org/10.2174/1381612053382287

Kumar, S., & Nussinov, R. (2002). Close-Range Electrostatic Interactions in Proteins. *ChemBioChem*, *3*(7), 604. https://doi.org/10.1002/1439-7633(20020703)3:7<604::AID-CBIC604>3.0.CO;2-X

Lenard, J., Rabson, A., & Vanderoef, R. (1993). Photodynamic inactivation of infectivity of human immunodeficiency virus and other enveloped viruses using hypericin and rose bengal: Inhibition of fusion and syncytia formation. *Proceedings of the National Academy of Sciences of the United States of America*, *90*(1), 158–162. https://doi.org/10.1073/pnas.90.1.158

Lopes, B. R. P., da Costa, M. F., Genova Ribeiro, A., da Silva, T. F., Lima, C. S., Caruso, I. P., de Araujo, G. C., Kubo, L. H., Iacovelli, F., Falconi, M., Desideri, A., de Oliveira, J., Regasini, L. O., de Souza, F. P., & Toledo, K. A.

(2020). Quercetin pentaacetate inhibits in vitro human respiratory syncytial virus adhesion. *Virus Research*, *276*(May 2019), 197805. https://doi.org/10.1016/j.virusres.2019.197805

Martínez, L., Andrade, R., Birgin, E. G., & Martínez, J. M. (2009). PACKMOL: A package for building initial configurations for molecular dynamics simulations. *Journal of Computational Chemistry*, *30*(13), 2157–2164. https://doi.org/10.1002/jcc.21224

Martyna, G. J., Tobias, D. J., & Klein, M. L. (1994). Constant pressure molecular dynamics algorithms. *The Journal of Chemical Physics*, *101*(5), 4177–4189. https://doi.org/10.1063/1.467468

Matos, A. da R., Caetano, B. C., de Almeida Filho, J. L., Martins, J. S. C. de C., de Oliveira, M. G. P., Sousa, T. das C., Horta, M. A. P., Siqueira, M. M., & Fernandez, J. H. (2022). Identification of Hypericin as a Candidate Repurposed Therapeutic Agent for COVID-19 and Its Potential Anti-SARS-CoV-2 Activity. *Frontiers in Microbiology*, *13*(February), 1–11. https://doi.org/10.3389/fmicb.2022.828984

Miao, Y., Feher, V. A., & McCammon, J. A. (2015). Gaussian Accelerated Molecular Dynamics: Unconstrained Enhanced Sampling and Free Energy Calculation. *Journal of Chemical Theory and Computation*, *11*(8), 3584–3595. https://doi.org/10.1021/acs.jctc.5b00436

Mohamed, F. F., Anhlan, D., Schöfbänker, M., Schreiber, A., Classen, N., Hensel, A., Hempel, G., Scholz, W., Kühn, J., Hrincius, E. R., & Ludwig, S. (2022). Hypericum perforatum and Its Ingredients Hypericin and Pseudohypericin Demonstrate an Antiviral Activity against SARS-CoV-2. *Pharmaceuticals*, *15*(5). https://doi.org/10.3390/ph15050530

Nikolaeva-Glomb, L., Mukova, L., Nikolova, N., Kussovski, V., Doumanova, L., Mantareva, V., Angelov, I., Wöhrle, D., & Galabov, A. S. (2017). Photodynamic effect of some phthalocyanines on enveloped and naked viruses. *Acta Virologica*, *61*(3), 341–346. https://doi.org/10.4149/av_2017_313

Pan, B. W., Xiao, J. W., Li, S. M., Yang, X., Zhou, X., Sun, Q. W., Chen, M., Xie, S. X., Sakharkar, M. K., Yang, J., Zhou, Y., & Wei, Y. (2022). Inhibitors of HIV-1 and Cathepsin L Proteases Identified from the Insect Gall of Hypericum kouytchense. *Pharmaceuticals*, *15*(12). https://doi.org/10.3390/ph15121499

Parrinello, M., & Rahman, A. (1981). Polymorphic transitions in single crystals: A new molecular dynamics method. *Journal of Applied Physics*, *52*(12), 7182–7190. https://doi.org/10.1063/1.328693

Pezeshkian, W., Grünewald, F., Narykov, O., Lu, S., Wassenaar, T. A., Marrink, S. J., & Korkin, D. (2021). Molecular architecture of SARS-CoV-2 envelope by integrative modeling. *BioRxiv*, 2021.09.15.459697. https://www.biorxiv.org/content/10.1101/2021.09.15.459697v1%0Ahttps://www.biorxiv.org/content/10.1101/2021.09.15.459697v1.abstract

Phillips, J. C., Braun, R., Wang, W., Gumbart, J., Tajkhorshid, E., Villa, E., Chipot, C., Skeel, R. D., Kalé, L., & Schulten, K. (2005). Scalable molecular dynamics with NAMD. *Journal of Computational Chemistry*, *26*(16), 1781–1802. https://doi.org/10.1002/jcc.20289

Romeo, A., Iacovelli, F., & Falconi, M. (2020). Targeting the SARS-CoV-2 spike glycoprotein prefusion conformation: virtual screening and molecular dynamics simulations applied to the identification of potential fusion inhibitors. *Virus Research*, *286*(June), 198068. https://doi.org/10.1016/j.virusres.2020.198068

Saadi, F., Pal, D., & Sarma, J. Das. (2021). Spike Glycoprotein Is Central to Coronavirus Pathogenesis-Parallel Between m-CoV and SARS-CoV-2. *Annals of Neurosciences*, *28*(3–4), 201–218. https://doi.org/10.1177/09727531211023755

Santos, K. L. M., Barros, R. M., da Silva Lima, D. P., Nunes, A. M. A., Sato, M. R., Faccio, R., de Lima Damasceno, B. P. G., & Oshiro-Junior, J. A. (2020). Prospective application of phthalocyanines in the photodynamic therapy

against microorganisms and tumor cells: A mini-review. *Photodiagnosis and Photodynamic Therapy*, *32*(August), 102032. https://doi.org/10.1016/j.pdpdt.2020.102032

Sen, C. K., & Packer, L. (1996). Antioxidant and redox regulation of gene transcription. *The FASEB Journal*, *10*(7), 709–720. https://doi.org/10.1096/fasebj.10.7.8635688

Smetana, Z., Mendelson, E., Manor, J., van Lier, J. E., Ben-Hur, E., Salzberg, S., & Malik, Z. (1994). Photodynamic inactivation of herpes viruses with phthalocyanine derivatives. *Journal of Photochemistry and Photobiology, B: Biology*, *22*(1), 37–43. https://doi.org/10.1016/1011-1344(93)06949-4

Smith, M., & Smith, J. C. (2020). Repurposing Therapeutics for COVID-19: Supercomputer-Based Docking to the SARS-CoV-2 Viral Spike Protein and Viral Spike Protein-Human ACE2 Interface. *ChemRxiv*, *2*. https://doi.org/doi.org/10.26434/chemrxiv.11871402.v4

Sorokin, A. B. (2013). Phthalocyanine Metal Complexes in Catalysis. *Chemical Reviews*, *113*(10), 8152–8191. https://doi.org/10.1021/cr4000072

Souza, P. C. T., Alessandri, R., Barnoud, J., Thallmair, S., Faustino, I., Grünewald, F., Patmanidis, I., Abdizadeh, H., Bruininks, B. M. H., Wassenaar, T. A., Kroon, P. C., Melcr, J., Nieto, V., Corradi, V., Khan, H. M., Domański, J., Javanainen, M., Martinez-Seara, H., Reuter, N., … Marrink, S. J. (2021). Martini 3: a general purpose force field for coarse-grained molecular dynamics. *Nature Methods*, *18*(4), 382–388. https://doi.org/10.1038/s41592-021-01098-3

Souza, P. C. T., Thallmair, S., Conflitti, P., Ramírez-Palacios, C., Alessandri, R., Raniolo, S., Limongelli, V., & Marrink, S. J. (2020). Protein–ligand binding with the coarse-grained Martini model. *Nature Communications*, *11*(1), 1–11. https://doi.org/10.1038/s41467-020-17437-5

Stevenson, N. R., & Lenard, J. (1993). Antiretroviral activities of hypericin and rose bengal: Photodynamic effects on Friend leukemia virus infection of mice. *Antiviral Research*, *21*(2), 119–127. https://doi.org/10.1016/0166-3542(93)90048-N

Tang, T., Bidon, M., Jaimes, J. A., Whittaker, G. R., & Daniel, S. (2020). Coronavirus membrane fusion mechanism offers a potential target for antiviral development. *Antiviral Research*, *178*(January), 104792. https://doi.org/10.1016/j.antiviral.2020.104792

Telenti, A., Arvin, A., Corey, L., Corti, D., Diamond, M. S., García-Sastre, A., Garry, R. F., Holmes, E. C., Pang, P. S., & Virgin, H. W. (2021). After the pandemic: perspectives on the future trajectory of COVID-19. *Nature*, *596*(7873), 495–504. https://doi.org/10.1038/s41586-021-03792-w

Vanommeslaeghe, K., Hatcher, E., Acharya, C., Kundu, S., Zhong, S., Shim, J., Darian, E., Guvench, O., Lopes, P., Vorobyov, I., & Mackerell, A. D. (2010). CHARMM general force field: A force field for drug-like molecules compatible with the CHARMM all-atom additive biological force fields. *Journal of Computational Chemistry*, *31*(4), 671–690. https://doi.org/10.1002/jcc.21367

Vzorov, A. N., Marzilli, L. G., Compans, R. W., & Dixon, D. W. (2003). Prevention of HIV-1 infection by phthalocyanines. *Antiviral Research*, *59*(2), 99–109. https://doi.org/10.1016/S0166-3542(03)00035-4

Wang, B., Zhong, C., & Tieleman, D. P. (2022). Supramolecular Organization of SARS-CoV and SARS-CoV-2 Virions Revealed by Coarse-Grained Models of Intact Virus Envelopes. *Journal of Chemical Information and Modeling*, *62*(1), 176–186. https://doi.org/10.1021/acs.jcim.1c01240

Wang, J., Arantes, P. R., Bhattarai, A., Hsu, R. V., Pawnikar, S., Huang, Y. M., Palermo, G., & Miao, Y. (2021). Gaussian accelerated molecular dynamics: Principles and applications. *WIREs Computational Molecular Science*, *11*(5), 1–32. https://doi.org/10.1002/wcms.1521

900 Wassenaar, T. A., Ingólfsson, H. I., Böckmann, R. A., Tieleman, D. P., & Marrink, S. J. (2015). Computational lipidomics
901 with insane: A versatile tool for generating custom membranes for molecular simulations. *Journal of Chemical*
902 *Theory and Computation*, *11*(5), 2144–2155. https://doi.org/10.1021/acs.jctc.5b00209
903 Weber, N. D., Murray, B. K., North, J. A., & Wood, S. G. (1994). The antiviral agent hypericin has in vitro activity
904 against HSV-1 through non-specific association with viral and cellular membranes. *Antiviral Chemistry and*
905 *Chemotherapy*, *5*(2), 83–90. https://doi.org/10.1177/095632029400500204
906 Woo, H., Park, S. J., Choi, Y. K., Park, T., Tanveer, M., Cao, Y., Kern, N. R., Lee, J., Yeom, M. S., Croll, T. I., Seok, C.,
907 & Im, W. (2020). Developing a Fully Glycosylated Full-Length SARS-CoV-2 Spike Protein Model in a Viral
908 Membrane. *The Journal of Physical Chemistry. B*, *124*(33), 7128–7137. https://doi.org/10.1021/acs.jpcb.0c04553
909 Wright, J. D. (2001). Phthalocyanines. In *Encyclopedia of Materials: Science and Technology* (pp. 6987–6991). Elsevier.
910 https://doi.org/10.1016/B0-08-043152-6/01238-9
911 Wu, J.-J., Zhang, J., Xia, C.-Y., Ding, K., Li, X.-X., Pan, X.-G., Xu, J.-K., He, J., & Zhang, W.-K. (2023). Hypericin: A
912 natural anthraquinone as promising therapeutic agent. *Phytomedicine : International Journal of Phytotherapy and*
913 *Phytopharmacology*, *111*(January), 154654. https://doi.org/10.1016/j.phymed.2023.154654
914 Xiu, S., Dick, A., Ju, H., Mirzaie, S., Abdi, F., Cocklin, S., Zhan, P., & Liu, X. (2020). Inhibitors of SARS-CoV-2 Entry:
915 Current and Future Opportunities. *Journal of Medicinal Chemistry*, *63*(21), 12256–12274.
916 https://doi.org/10.1021/acs.jmedchem.0c00502
917 Yu, A., Pak, A. J., He, P., Monje-Galvan, V., Casalino, L., Gaieb, Z., Dommer, A. C., Amaro, R. E., & Voth, G. A.
918 (2021). A multiscale coarse-grained model of the SARS-CoV-2 virion. *Biophysical Journal*, *120*(6), 1097–1104.
919 https://doi.org/10.1016/j.bpj.2020.10.048
920
921

FIGURES CAPTIONS

Figure 1. On the right, last frames extracted from the GaMD trajectories representing the insertion of one phthalocyanine (A) and two hypericin molecules (B) within the viral bilayer. The C-terminal region of the S protein is shown as a grey cartoon, while the compounds are shown as spacefill coloured by atom type. Membrane lipid tails are represented as grey transparent sticks, while their polar heads are shown as red spheres. 2D structures of the compounds are also represented. On the left, thickness heatmaps calculated for the viral membrane in the phthalocyanine, hypericin and reference systems. Black circles indicate molecules' insertion regions.

Figure 2. (A) Four hypericin molecules, represented as spheres coloured by atom type, binding at the three S RBDs, shown as blue surfaces. The RBM regions are highlighted in green. Other S regions are shown as grey cartoons. (B) The two hypericin molecules located outside the HR1 domains (blue), facing the internal pocket of the protein and contacting the fusion peptide (green). The HR1 domain and fusion peptides are shown as surface, while the rest of the protein is shown as a grey cartoon. (C) Hypericin molecules binding to the S HR2 domains (green surface). The membrane is represented as sticks, with polar heads coloured in red and lipid tails shown in brown.

Figure 3. (A) Volumetric maps, represented by grid isosurfaces, indicating main binding regions of hypericin molecules on the S protein. Different colours identify the 14 replicas. (B, C) Closer view of the volumetric maps obtained for the hypericin molecules around: (B) the protein RBDs and (C) HR1 and fusion peptides domains. The same colour coding described in Figure 2 has been applied. Grey lines represent the CG protein elastic network.

Figure 4. (A-D) Hypericin molecules binding within the S internal pocket, identified in 4 of 14 replicas. The protein elastic network is shown as grey wires and backbone beads as orange spheres. Hypericin molecules are shown as spheres coloured by bead type.

Figure 5. (A) ROS measures performed after HEK293T-ACE2 cells incubation with a solution of DCF at 37 °C for 1 h in the dark. Cells were treated with hypericin or phthalocyanine at two different concentrations (C1: 0.78 μg/ml and C2: 0.005 μg/ml). Two experimental conditions (manipulation in the dark or light) have been compared. DCF oxidation was determined by fluorimetric measurement of fluorescence (excitation 488nm, emission 530 nm). Both negative (untreated cells) and positive (cells treated with 100μM menadione for one hour) controls have been included in all the experimental conditions. Results are expressed as average ± SD of triplicate values and are representative of five different experiments by Student's t test (****P <0.0001). (B) Results of the infection assays performed using a SARS-CoV-2 pseudovirus and HEK293T cells transfected with ACE2. Data were obtained after cell infection by luciferase measurement through a luminometer and

955 are expressed in RLU (Relative Light Unit). Results are representative of three different series of
956 experiments using two different compounds concentration in the three experimental conditions: (I)
957 pre-treatment of PSV with CP (HYP or PHT); (II) pre-treatment of HEK293T cells with CP (HYP or
958 PHT); (III) CP-PSV - HEK293T co-treatment. Negative control corresponds to both untreated and
959 non-infected cells. Positive control corresponds to only infected cells. Results are expressed as
960 average ± SD of triplicate values and are representative of three different experiments by Welch‘s t
961 test (****P <0.0001). HYP: hypericin, PHT: phthalocyanine. PSV pseudovirus, CP compounds.

962
963
964
965
966
967
968
969
970
971
972
973
974
975
976
977